Korean J. Chem. Eng., 40(5), 1186-1196 (2023)
DOI: 10.1007/s11814-022-1299-5

pISSN: 0256-1115
eISSN: 1975-7220

Synergistic impact of multiwalled carbon nanotubes on the properties of Ni-Mo thin-film via electrodeposition technique

Mona Hasan Gomaa*, Zeinab Abdel Hamid*,†, Magdy Ahmed Mahmoud Ibrahim, Rania Abd El Sttar**, and El-Said Helmy El- Mosallamy****

*Corrosion Control and Surface Protection Department, Central Metallurgical Research
and Development Institute (CMRDI), Cairo, Egypt
**Chemistry Department, Faculty of Science, Ain Shams University, Cairo, 11566, Egypt

(*Received 27 June 2022 • Revised 18 September 2022 • Accepted 23 September 2022*)

Abstract−Carbon nanotubes (CNTs) are the hardest and strongest materials due to their perfect mechanical properties and excellent chemical, electrical, and thermal characteristics. Therefore, CNTs are attractive candidates for the development of innovative multifunctional nanocomposites. The goal of the study was to synthesize and characterize NiMoCNT nanocomposite coatings onto steel substrates by electrodeposition technique to enhance the properties of the NiMo layer coating. The electrodeposition was carried out galvanostatically, and the percentage of MWCNT (wt%) in the composites was investigated under various working circumstances, including current density, pH, temperature, and CNTs concentration in the electroplating bath. Different techniques, such as X-ray diffraction (XRD), X-ray photoelectron spectroscopy (XPS), and energy dispersive X-ray analysis (EDS) ,were used for the composite characterization. Moreover, the corrosion resistance and the nanocomposites' mechanical characteristics were investigated. The results of the NiMo alloy show that the enhancement in current density decreases the Mo content from 41.8 wt% (at 3.5×10^{-2} Acm^{-2}) to 31.06 wt% (at 6.5×10^{-2} Acm^{-2}). On the other hand, the results proved that as the concentration of CNTs in the bath increases, the wt% of CNTs co-deposited in the NiMo matrix enhances, peaking at 22.36 wt% at 0.03 gL^{-1}. Furthermore, the findings show that the Mo content of the coating is reduced when CNTs are present. In comparison to a NiMo coating without CNTs, the composite incorporating CNTs exhibits better corrosion resistance. In addition, the mechanical properties show that the microhardness of NiMoCNT composite-coated steel is better than that of NiMo, and the highest microhardness of NiMoCNT composite coated steel was 4.69 GPa, while pure NiMo coated steel had a microhardness of 2.37 GPa.

Keywords: NiMoCNTs, Nano-composite, Electrodeposition, Impedance, Polarization, Nanoindentation

INTRODUCTION

Owing to their ideal atomic structure and intrinsic tight in-plane sp^2-sp^2 covalent bonds between carbon atoms, carbon nanotubes (CNTs) are the toughest and strongest materials. CNTs also have outstanding mechanical, chemical, electrical, and thermal properties [1]. Because of their chemical stability, CNTs can be utilized to fabricate composites with promising corrosion resistance and high hardness [2-4]. MWCNTs, especially with Mo alloys, have a wide range of other uses, including the production of transistors, voltage inverters, sensors, field emission sources, and energy storage devices [5,6]. One of the most effective stable electrocatalysts for the oxygen evolution reaction (OER) and hydrogen evolution reaction (HER) is $Mo_{0.29}Co_{0.71}P_2$/MWCNTs [7]. On the other hand, a composite of $MoSe_2$/MWCNTs has been developed for supercapacitor applications [8].

A number of factors can affect the effectiveness of codeposition and the quality of the composites it produces, including particle size and bath concentration [9]. Several efforts have been made to develop composites with different matrices of nanotubes and nanofibers [10]. Different preparation techniques were investigated for producing composite materials, such as plasma spray [11], sol-gel [12], electroless [13,14], and electrodeposition. Electrodeposition is among these techniques one of the most cost-effective methods for achieving composite metal matrix coatings [15]. The electrochemical co-deposition approach has been used to generate metallic coatings using both single-walled carbon nanotubes (SWCNT) and multi-walled carbon nanotubes (MWCNT). To improve the mechanical and corrosion properties of composite coatings, ceramic particles such as SiC, TiO_2, CeO_2, ZnO, and Al_2O_3 are commonly used [16-18]. Recently, Sm_2O_3 was introduced into the matrix of ZnNi alloy to improve its corrosion as well as its microhardness properties [19]. The metal matrix is made up of pure metals like Ni, Cu, and Cr, as well as alloys like ZnNi [20], NiCu [21], NiW [22].

Molybdenum increases the properties of metal coatings as an alloy component by enhancing hardness, abrasion resistance, and corrosion resistance. Just a few papers on the use of a molybdenum-containing alloy matrix can be found in the literature. The H_2 discharge reaction on a Ni-based composite coating incorporating Mo powder was explored by Kubisztal [23]. Chen studied the H_2 evolution catalysts based on NiMoN nanosheets [24]. Therefore, the work aimed to synthesize NiMoCNTs composite via an electrode-

---

† To whom correspondence should be addressed.

E-mail: forzeinab@yahoo.com

Table 1. The chemical composition and experimental parameters of NiMoCNTs bath

Constituents of NiMoCNTs bath (g/L)		Experimental parameters	
Nickel sulphate hexahydrate ($NiSO_4 \cdot 6H_2O$)	31	pH	3.5
Sodium molybdate ($Na_2MoO_4 \cdot 2H_2O$)	8	Temperature	25 °C
Glycine ($C_2H_5NO_2$)	100	Current density (c.d.)	$\times 10^{-2}$
Sodium dodecyl sulphate surfactant ($NaC_{12}H_{25}SO_4$)	0.001	Acm^{-2}	3.5-6.5
MWCNT (0-0.03)	(0-0.03)	Deposition time, min	30

position technique and investigate its characterization. The nanocomposite was subjected to tests for thickness, microhardness, and corrosion resistance. In addition, the electrochemical behavior and kinetics of MWCNT incorporation into the NiMo coating were investigated.

MATERIAL AND METHODS

All the plating and chemical reagents were made from nickel sulfate hexahydrate (Bio tech), glycine, sodium molybdate, sodium dodecyl sulphate (ADWIC), and graphene supermarket (Multi-walled carbon nanotube powder). The pH of each bath was detected utilizing a pH meter (Adwa AD1000). The pH meter was tested using buffer solutions with precise pH values. By adding a 1 : 3 H_2SO_4 solution to the electrolyte, the pH was regulated. The chemical composition of the baths used for NiMoCNT composite electrodeposition and the conditions are mentioned in Table 1.

All the electrodes used in the electrodeposition (cathode and anode) were in the form of sheets: the cathode is a steel sheet with a dimension of 30×30×1 mm and the anode is a Pt sheet with a dimension of 30×30×0.3 mm. The steel cathodes were mechanically polished with emery papers ranging in grade from 230 to 1,000, and then rinsed with distilled water. After that, they were dried with tissue or paper towel, then put in the desiccators to dry completely, and finally weighed and dipped in the plating cell. A magnetic agitator at 600 rpm was used to agitate the CNTs composite coating solution for approximately 8 hours before electroplating. It was then ultrasounded for approximately 30 minutes. The temperature was held at 25 °C during agitation. A regulated DC power supply was used to perform the electrochemical deposition.

For the electrochemical measurement, the reference electrode was Ag/AgCl, the counter electrode was a platinum sheet, and the working electrode was a Pt disc electrode (PtDE). It was cleaned with Al_2O_3 powder until a mirror surface was achieved before each experiment, then washed multiple times with distilled water. The i/E curves were measured potentiodymically. Before every experiment, the electrolytic cell was cleansed and filled to a specific level with the test plating solution to ensure that the electrodes were completely submerged. Then the cleaned electrodes were placed in their respective positions. In potentiatodynamics measurements, the cathodic potential changed automatically from its static potential Es with respect to the reference electrode towards more negative potential values with a sweep rate of 5 mVs^{-1}, and the associated flowing current was traced as a function of potential.

Anodic linear stripping voltammetry (ALSV) was done as described earlier [25]. The current-time transient was recorded at a given cathodic deposition for a certain deposition time (at a constant MWCNT content in the plating solution), and other series were carried out at different MWCN concentrations in the plating solution at constant deposition potential (−0.85 V).

The XRD patterns of the NiMoCNTs nanocomposite were investigated using an X'Pert Pro powder diffractometer within a diffraction angle range of 4-80, operating with CuKα radiation (40 mA and 45 kV). A scanning electron microscope (SEM-JEOL-5410) with an energy dispersive X-ray analyzer was used to investigate the components of the electrodeposited layers (EDX). The produced samples were examined using a Thermo Scientific K-alpha XPS machine (Waltham, MA, USA). To acquire chemical state information, the sample was irradiated with a monochromatic Al K X-ray source, and the analyzer passed an energy of 200 eV with a step size of 1 eV for high-resolution spectra.

With a Berkovich indenter, nanoindentation (Micro Materials, UK) was utilized to investigate the mechanical characteristics of the coating under depth versus load hysteresis testing circumstances. The loading rate is 2.5 mN/s, unloading rate is 2.5 mN/s, limit stop load (0.1 mN), initial load (0.05 mN), loading time (20 s), unloading time (40 s), dwell period at maximum load (10 s), and retraction distance were all measured with a minimum load of 10 mN and a maximum load of 10 mN to minimize the substrate effects.

RESULTS AND DISCUSSION

Preliminary experiments for the electrodeposition of NiMo alloy onto steel substrate were carried out to achieve a suitable bath composition as well as suitable operating conditions to produce satisfactory deposition coatings. Therefore, it was found that the chemical composition as shown in Table 1 is the suitable bath composition for the deposition at pH 3.5.

1. Electrodeposition Process

The influence of current density on the coating thickness of NiMo and NiMoCNTs deposited coatings is shown in Fig. 1(A). The coating thickness increased as the current density (c.d.) increased due to improvements in cathodic current efficiency. The maximum c.d. is attained when the rate of Ni and Mo ions transiting from the bulk to the cathode surface is combined with the deposition rate. Furthermore, low c.d. (3.50×10^{-2} Acm^{-2}) results in very little deposition, whereas high c.d. ($>5.5\times10^{-2}$ Acm^{-2}) results in a rapid increase in hydrogen evolution, which inhibits deposit adhesion. Moreover, Fig. 1(A) shows the variation in the current density and the composite coating thickness at different CNTs concentrations. It is clear that at any c.d. up to 5.5×10^{-2} Acm^{-2}, when the concentration of CNTs increases, the coating thickness decreases compared with that formed without CNTs. While at a higher current density than 5.5×10^{-2} Acm^{-2}, this concept is not valid. It may

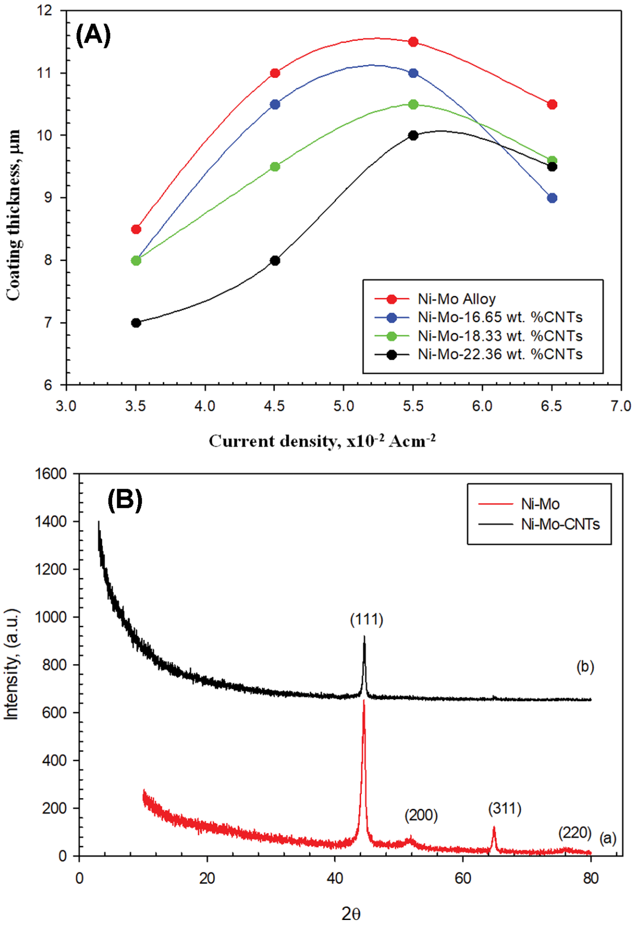

Fig. 1. (A) The relation between the current density and the coating thickness of NiMo alloy in the absence and presence of different MWCNT content deposited at room temperature, and (B) XRD patterns of NiMo (a) and NiMo-22.36 wt%CNTs (b) film deposited layer at the optimum condition (5.5×10^{-2} Acm^{-2}, at 25 °C, duration time 30 min and 0.02 gL^{-1} CNTs in the electrolyte).

be due to the partial peel off and, consequently, low adhesion of the formed layer is expected.

2. Characterization of the Nano-composite

2-1. EDX and XRD Analysis

The presence of various elements in the coatings was determined using EDX analysis. The composition of NiMo coatings at various current densities is shown in Table 2. The impact of CNT content in the bath on CNTs wt% in the NiMo alloy deposited at the optimum current density of 5.5×10^{-2} Acm^{-2} was also investigated. The data in Table 2 shows that the c.d. has a significant impact on the composition of the coatings. The c.d. had a significant impact on the coating's Mo content. It should be noticed that increasing c.d. from 3.5×10^{-2} to 6.5×10^{-2} Acm^{-2} resulted in a reduction in Mo content from 41.8 wt% (at 3.5×10^{-2} Acm^{-2}) to 31.06 wt% (at 6.5×10^{-2} Acm^{-2}). Thus, the peculiar behavior of Mo content fluctuation with c.d. could be related to metal ion complexation, which has a major impact on the parent metals' static potentials. Thus, due to a poor rate of mass transport of electroactive species (Mo^{+2} ions) from a pH-dependent molybdate-glycine complex, the bath has a very low partial current density for Mo deposition (relative to its estimated limiting current density). As a result, the drop in Mo content with c.d. is due to a change in current density (due to H_2 evolution), which causes the equilibrium of its glycine complex to shift, rather than a change in its limiting current density, which is consistent with Liu et al. [26].

Molybdenum cannot be electrodeposited in its metallic state from an aqueous solution, but it can be co-deposited with Fe-group elements to form an alloy. The above phenomenon is known as induced co-deposition. Individual metal behavior in induced co-deposition is erratic and difficult to predict, reflecting the intricate alloy production mechanism. The reduction of Ni(II) and Mo(VI) complex ions, as well as H_2 evolution, occurs simultaneously during the process. Low valence state oxides of molybdenum may form in the generated films in addition to the induced co-deposition of metallic molybdenum. On the other hand, the findings illustrate that as the concentration of CNTs in the electrolyte increases, the weight percent of CNTs co-deposited into the NiMo matrix increases as well, peaking at 22.36 wt% at 0.03 gL^{-1}. Moreover, the data in Table 2 shows that CNTs content has a decreasing impact on the Mo content of the coating.

Fig. 1(B) shows XRD patterns of NiMo (a) and NiMoCNTs (b) coatings. It is clear that in the NiMo alloy pattern (a), diffraction peaks for the NiMo lattice plane are located at 2θ~44°, 52°, 65°, and 75°, which relates to the following planes: (111), (200), (311), and (220), respectively, seem to be slightly shifted, and the intensity decreases. While in the NiMoCNTs coating, all the peaks in the chart disappear except the lattice plane (111), as explored in Fig. 1((B)-(b)). The peak intensity at 44° was clearly the most common, indicating that the electrodeposited NiMo and NiMoCNTs coat-

Table 2. The composition of the NiMo and NiMoCNTs composite coatings at different current densities and MWCNTs contents

Sample	Current density, $*10^{-2}$ Acm^{-2}											
NiMo	3.5		4.5		5.5		6.5					
Wt%	Ni	Mo	Ni	Mo	Ni	Mo	Ni	Mo				
	58.2	41.8	59.3	40.7	68.6	31.9	68.9	31.1				
	Content of MWCNTs, g/L											
NiMoCNTs	0.01				0.02				0.03			
Wt%	Ni	Mo	Fe	C	Ni	Mo	Fe	C	Ni	Mo	Fe	C
	45.34	30.36	7.65	16.65	48.19	24.57	8.91	18.33	45.88	23.66	8. 10	22.36

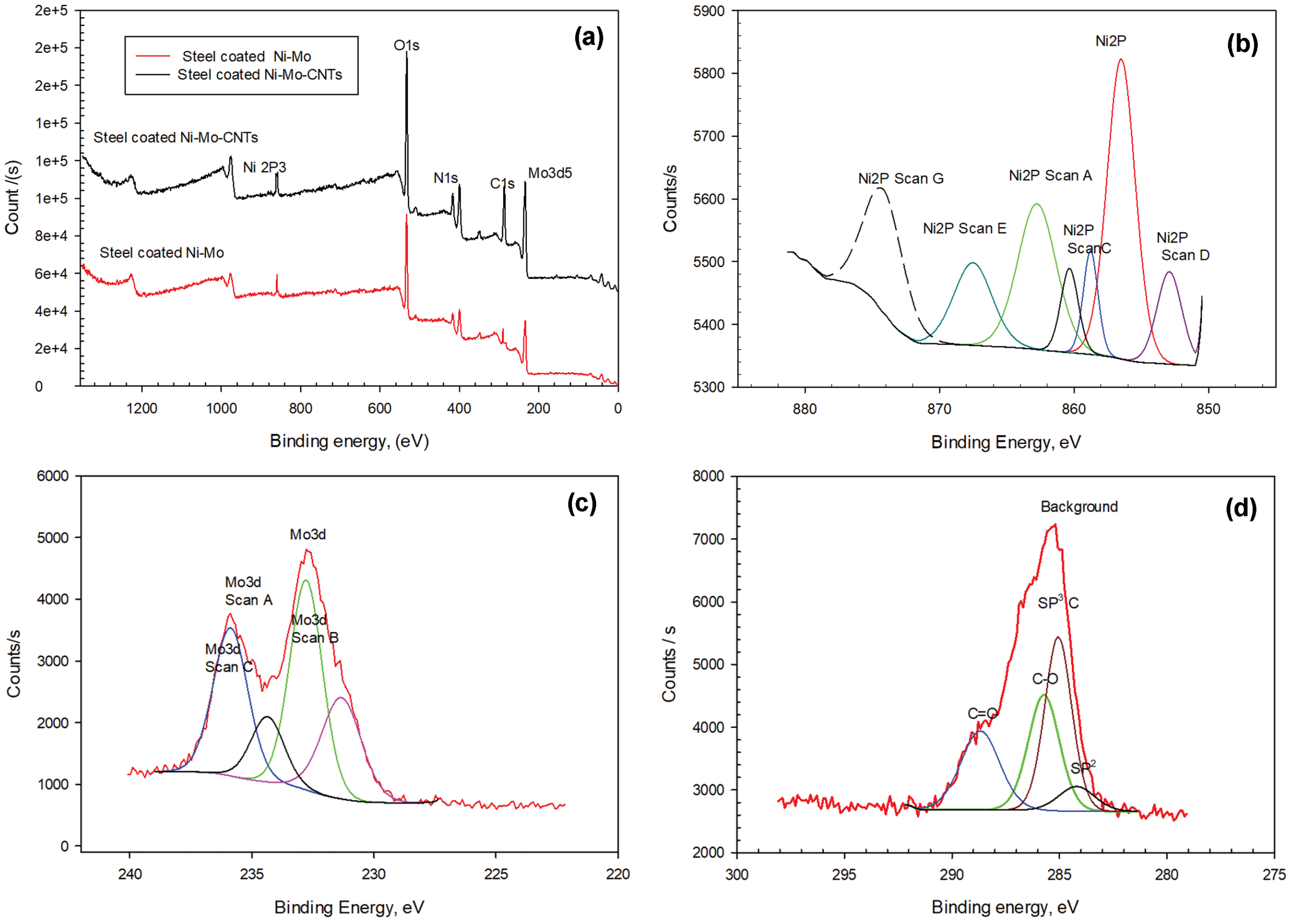

Fig. 2. (a) XPS of the NiMo and NiMo 22.36 wt% CNT's deposited layer at optimum conditions (5.5×10^{-2} Acm^{-2}, at room temperature, duration time 30 min, and 0.03 gl^{-1} CNTs), (b) Ni 2p spectra, (c) Mo3d5 spectra and (d) C1s spectra.

ings were made up of a one-phase NiMo solid solution with a fcc structure. It thus means that the reflection of the (111) plane indicates that the (111) growth direction becomes the preferred crystallographic direction during the CNTs incorporation. The result is in accord with Beltowaka-Lehman et al. [27], and Donten et al. [28].

2-2. XPS Analysis

The elemental chemical states in the NiMo and NiMoCNTs thin coatings were also determined using XPS analysis. XPS of the NiMo deposited coating operated at optimum condition (5.5×10^{-2} Acm^{-2}, at 25 °C, and duration time of 30 min) as well as NiMo-22.36 wt% CNT's deposited coating at the same optimum condition and 0.03 gL^{-1} CNT's content are shown in Fig. 2. C, O, Ni, and Mo peaks were discovered in the survey spectrum (Fig. 2(a)). The geometry of the Ni metal spectrum is complicated. The binding energies of Ni 2p are seen in high-resolution Ni XPS spectra (Fig. 2(b)) (856.49 eV); complex, multiplet-split peaks can also be found in Ni compounds (Scan A=862.75, Scan C=858.77, scan D=852.91, scan E=867.51, scan F=860.33, and scan G=874.17) for NiMo and NiMoCNTs. The high-resolution of Ni XPS spectra (Fig. 2(b)) show the binding energies of Ni 2p3/2 (+2=852.91, +3=858.77) and Ni 2p1/2 (+2=867.51, +3=874.17) for NiMo and NiMoCNTs coatings. Generally, Ni 2p3/2 and Ni 2p1/2 are responsible for the two peaks at 853.5 and 873.0 eV, respectively, whereas the satellite peaks are responsible for the other peaks [29]. The binding energy of Mo 3d can be seen in high-resolution Mo XPS spectra (Fig. 2(c)) (232.77 eV), Scan A=235.87 eV, Mo 3d Scan B=231.33 eV, and Mo 3d Scan C=234.36 eV. The high resolution Mo XPS spectra show the binding energy of Mo 3d3/2 (+6=235.87, +2=231.3) and Mo 3d5/2 (+6=234.36, +2=232.77) for NiMo and NiMoCNTs. The peak at 285.77 eV, which relates to the carbon in CNTs, is visible in a high-resolution spectra of C 1s (Fig. 2). Three peaks were found at about 284.25, 285.10, and 287.24 eV in Fig. 2(d) (analysis of C peaks), which were assigned to C-C, C-O, and C=O, subsequently.

3. Potentiodynamic Cathodic Polarization Curves

3-1. Effect of MWCNT Concentration

Potentiodynamic cathodic polarization (i/E) curves are highly crucial since they involve the characteristics of the entire deposition process. As a result, the i/E curves during NiMo electrodeposition were recorded at pH 3.5 and at 25 °C with and without varied amounts of MWCNT (Fig. 3(A)). The curves were swept in the negative direction at a scan rate of 5 mVs^{-1}. The pure nickel deposition curve is characterized by a quick potential shift to greater

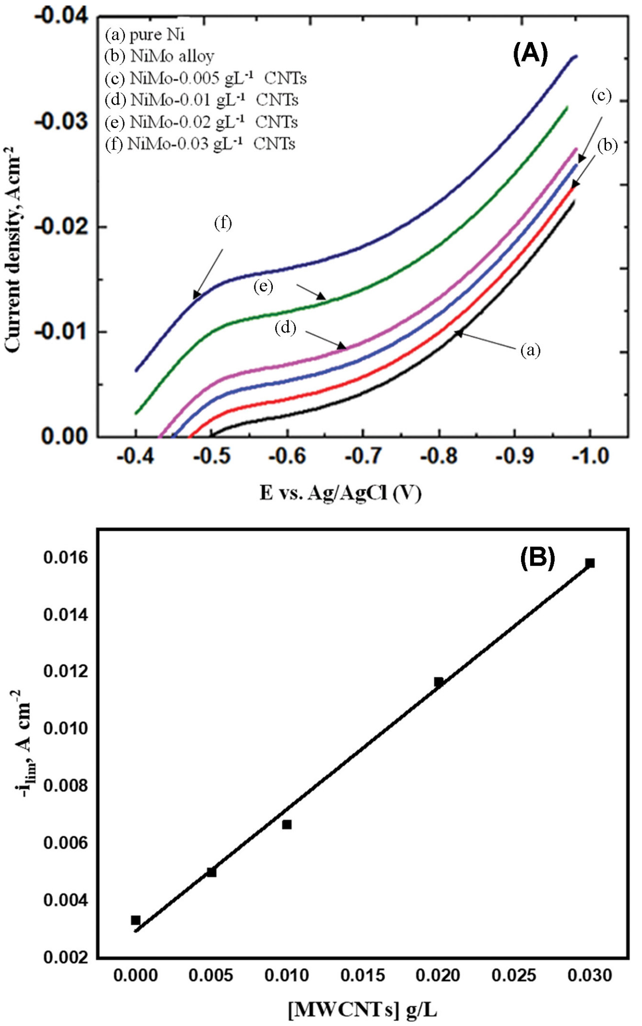

Fig. 3. **(A) Potentiodynamic cathodic polarization curves during NiMoCNT composite deposition containing different concentrations of CNT, scan rate=5 mVs^{-1} and 300 rpm, where (a) pure Ni, (b) NiMo alloy, (c), (d), (e)-(f) are NiMo with 0.005, 0.01, 0.02, 0.03 gL^{-1} MWCNT, respectively and (B) The relationship between i_{lim} and MWCNTs.**

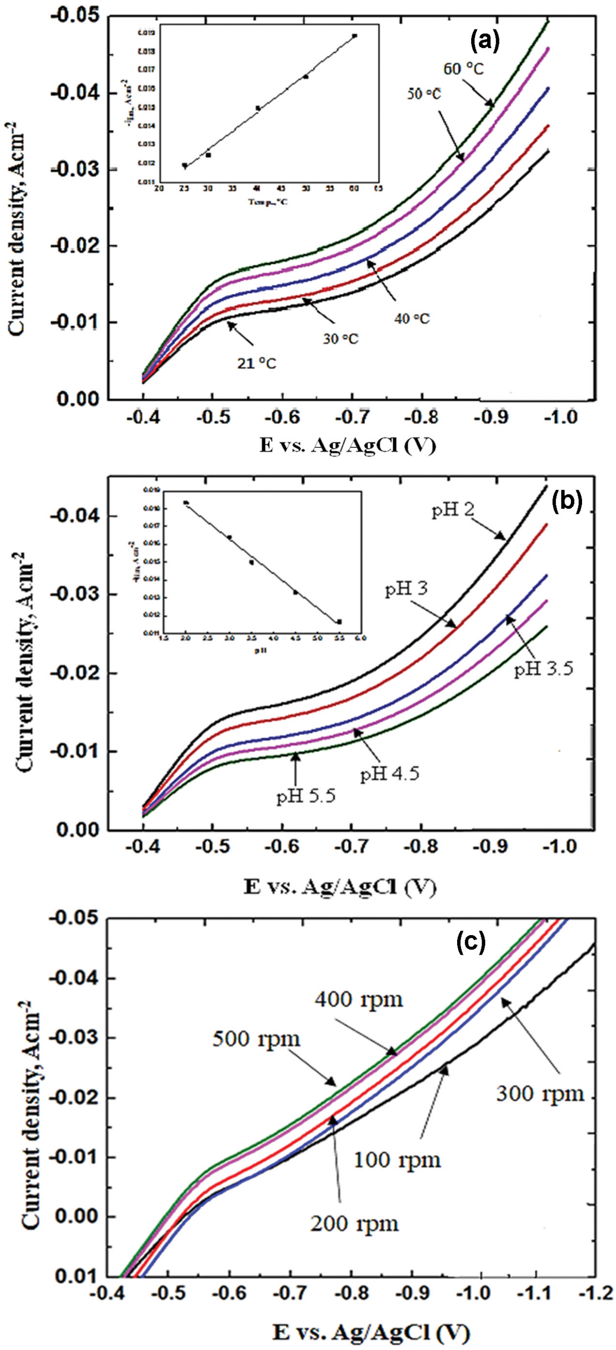

Fig. 4. **(a) The potentiodynamic cathodic polarization curves during composite deposition from the bath containing 0.02 gL^{-1} CNTs operated at a scan rate of 5 mVs^{-1}, 300 rpm and different temperatures, (b) at different pH values, and (c) at different stirring rate (rpm).**

negative values at first, followed by a continuous increase as current density increases. It thus shows that in the absence of Mo(VI) ions, nickel deposition is accompanied by a significant activation polarization [30]. However, when Mo(VI) is present in the electrolytic solution, the curve shifts to more noble potentials and is characterized by the presence of a limiting current plateau (i_{lim}), which is accentuated as the amount of MWCNTs in the bath increases. The above shift in the potential demonstrates that the presence of Mo(VI) facilitates the reduction of Ni^{2+} ions, and consequently increases the rate of their reduction. The relationship between i_{lim} (calculated from Fig. 3(A), at $-0.6\ V_{Ag/AgCl}$) and MWCNTs content in the bath is shown in Fig. 3(B). Under limiting conditions, the NiMo and the NiMoCNTs composite deposition proceeds via mass transfer control. Furthermore, during the deposition process, there was a simultaneous discharge of hydrogen ions. These findings further suggest that the presence of MWCNTs triggers the reduction of reducible ions, as evidenced by the significantly reduced current values observed. So, MWCNTs have a catalytic influence on Mo(VI) and Ni(II) reduction at the steel surface. A similar catalytic effect was observed for the reduction of Ni^{2+} and Zn^{2+} ions in the presence of Sm_2O_3 during the electrodeposition of ZnNi alloy [20].

3-2. The Influence of the Operating Temperature

The influence of temperature (25-60 °C) on the i/E curves is illustrated in Fig. 4(a) during the deposition of NiMoCNTs from the electrolyte containing a fixed concentration of MWCNT (0.02 g/L). Increasing the bath temperature causes a rise in i_{lim} as well as a notable move in the i/E curves towards more positive potentials due to its diminishing influence on the activation overvoltage for Mo(VI) and Ni(II) ions. Fig. 4(a) inset shows the relationship between i_{lim} and temperature. Additionally, increasing the bath temperature increases the diffusion coefficients of reducible species in the diffusion layer, which improves their concentration.

3-3. Effect of pH Values

The influence of pH value on the i/E curves during the deposition of NiMo (MWCNT 0.02 g/L) and at room temperature (25 °C) is displayed in Fig. 4(b). The polarization curves of the composite codeposition are found to be pH-dependent, with the curves shifting to greater negative potential values when the pH of the bath is increased. Furthermore, as shown in the inset of Fig. 4(b), as pH values increase, the i_{lim} decreases. The decrease in hydrogen overpotential is clearly responsible for the shift in polarization.

3-4. The Impact of the Stirring Rate

Fig. 4(c) shows the impact of stirring rate on the i/E curves during the deposition of NiMo from a bath containing a constant concentration of MWCNT (0.02 g/L), operated at 25 °C, and pH 3.5. The i/E curves shifted significantly to the more noble potential values as the stirring rate was increased, indicating an acceleration of Ni(II) and Mo(VI) ion deposition. It indicates that agitation accelerates the rate of NiMoCNTs deposition.

4. The Electrode Kinetics and the Tafel Lines

Tafel lines are created from the matching i/E curves (Fig. 3(B) and Fig. 4(a)-(c)) by graphing the logarithm of the current vs. the cathodic polarization according to the Tafel Eq. (1) to highlight the effect of MWCNTs and other parameters on the electrode kinetics.

$$\eta = a \pm \beta \log i \tag{1}$$

$$\beta = \frac{2.303RT}{\alpha nF} \tag{2}$$

where R is the gas constant, T is the temperature, F is the Faraday's constant, and α is the transfer coefficient.

Table 3 displays that in the presence of MWCNT, the cathodic Tafel slopes (β_c) and the exchange current density (i_0) increase, whereas the transfer coefficient (α) decreases. Practically, when additives or complexing agents are present in the solution, Tafel slopes are observed to be high [31]. The increase in i_o as MWCNTs are added shows that they have catalytic activity on the rate of com-

Table 3. The electrochemical parameters deduced from the polarization curve at a variable concentration of MWCNT (pH 3.5, 25 °C, and 300 rpm)

Content of CNTs, g/L	Exchange current density, i_o (A/cm^2)	Tafel slope $-\beta_c$ (mV/decade)	Transfer coefficient (α)
Ni	0.001242	0.4391	0.02924
NiMo alloy	0.001607	0.4879	0.02631
NiMo-0.005 CNT	0.002428	0.519	0.02474
NiMo-0.01 CNT	0.0028314	0.5565	0.02307
NiMo-0.02CNT	0.006561	0.700	0.02307
NiMo-0.03 CNT	0.008945	0.865	0.01484

Table 4. The electrochemical parameters deduced from the polarization curve at different temperatures (MWCNT 0.02 g/L, pH 3.5, and stirring rate 300 rpm)

Temp, °C	Exchange current density, i_o (A/cm^2)	Tafel slope $-\beta_c$ (mV/decade)	Transfer coefficient (α)
25	0.006561	0.7	0.02307
30	0.012823	0.785	0.01635
40	0.016406	0.845	0.01519
50	0.028314	0.914	0.01405
60	0.031696	0.956	0.01343

Table 5. The electrochemical parameters deduced from the polarization curve at variable stirring (MWCNT 0.02 g/L)

Stirring (rpm)	Exchange current density, i_o (A/cm^2)	Tafel slope $-\beta_c$ (mV/decade)	Transfer coefficient (α)
100	0.006592	0.797	0.01611
200	0.007586	0.806	0.01593
300	0.008035	0.9408	0.01365
400	0.010765	1.064	0.01207
500	0.011535	1.1165	0.0115

Table 6. The electrochemical parameters deduced from the polarization curve at variable pH (MWCNT 0.02 g/L)

pH	Exchange current density, i_o (A/cm^2)	Tafel slope $-\beta_c$ (mV/decade)	Transfer coefficient (α)
2.0	0.012023	0.824	0.01558
3.0	0.01122	0.789	0.01627
3.5	0.006561	0.700	0.02307
4.5	0.006053	0.659	0.01948
5.5	0.005445	0.569	0.02256

posite deposition. The conclusion is consistent with the polarization curve results previously mentioned (see Fig. 3(A)). Moreover, the same behavior has been illustrated by increasing the temperature and stirring rate (Tables 4 and 5). The impact of pH was studied, and the results are demonstrated in Table 6. The data affirms that increasing the pH values decreases both the i_o and the β_c, whereas increasing the pH values increases the α. All of that is supported further by polarization curves obtained at various pH levels, which show that as the pH rises, the polarization shifts to greater negative potential values, indicating a slower rate of composite deposition (see Fig. 4(b)). On other hand, enhancing the pH value increases the α considerably (Table 6). It also indicates that the increase in temperature and the stirring rate catalyze the electrodeposition process, while the increase in pH inhibits it.

5. Anodic Linear Stripping Voltammetry (ALSV)

The codeposition of the NiMoCNT composite on a PtDE at a constant deposition potential of −0.85 V Ag/AgCl for 100 seconds resulted in a series of ALSV measurements. Without withdrawing the electrode from the electrolyte (i.e., in situ) or altering the existing circumstances, the potential was scanned straight ahead in the noble direction with a scan rate of 5 mVs^{-1}, and an anodic stripping voltammogram was acquired immediately after composite plating. Figs. 5(A)-(C) provide some representative data. The influence of applying various concentrations of MWCNT on ALSV responses is depicted in Fig. 5(A). The ALSV has one anodic peak, corresponding to the dissolution of the deposited NiMo alloy. Despite their vastly different standard potentials, the Mo and Ni in the alloy dissolve together. In addition, increasing the MWCNT concentration in the bath enhances the area and height under the stripping peak, demonstrating that MWCNT has catalytic activity for NiMo alloy deposition. It is in accord with previous polarization curve results (see Fig. 3(A)). The role played by the pH on the ALSV is depicted in Fig. 5(B). The data demonstrates that as the pH of the bath rises, so does the quantity of electricity needed to form NiMoCNT nanocomposite, demonstrating that increasing the bath pH has a significant impact on NiMoCNT composite deposition. Additionally, Fig. 5(C) shows the effect of bath temperature (25-60 °C) on ALSV. As the bath temperature rises, the area and height beneath the stripping peak increase, indicating that a higher bath temperature supports catalytic activity for the deposition of NiMoCNT composite. The result is consistent with the earlier findings in Fig. 4(a).

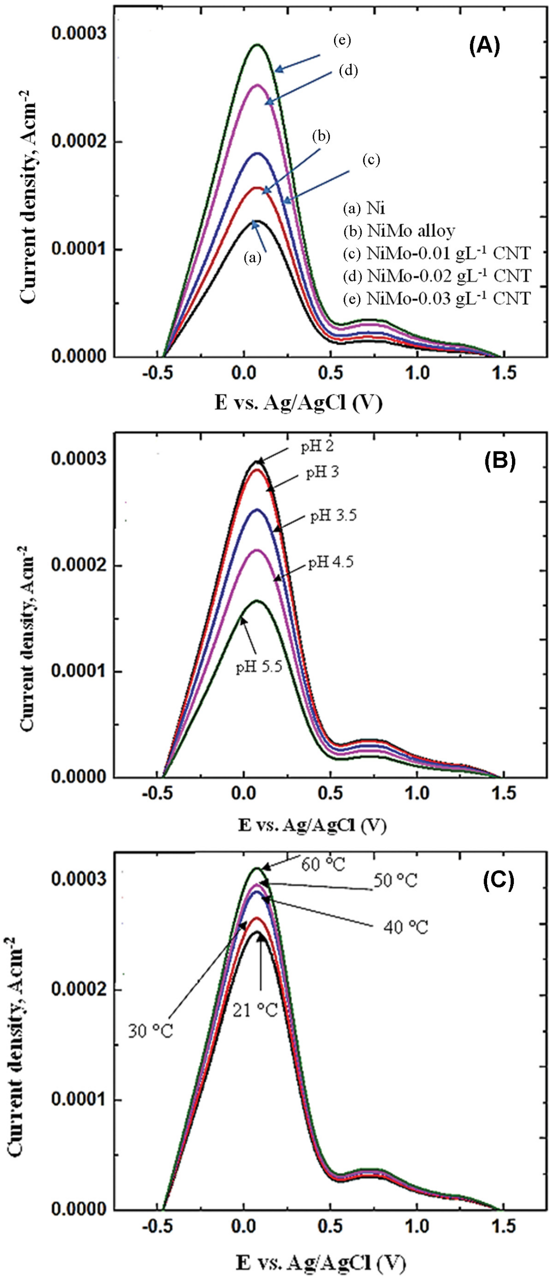

Fig. 5. (A) Anodic linear stripping voltammetric curve during NiMo alloy deposition in absence and presence different concentration of MWCNT, where (a) Ni only, (b) NiMo alloy, (c), (d) and (d) are 0.01, 0.02, 0.03 gL^{-1} MWCNT, respectively at 300 rpm, (B) at different pH values, and (C) at different temperature.

6. Chronamperometric Analysis

To learn more about the first nucleation and growth kinetic processes of NiMoCNT composite formation, researchers used chrono-

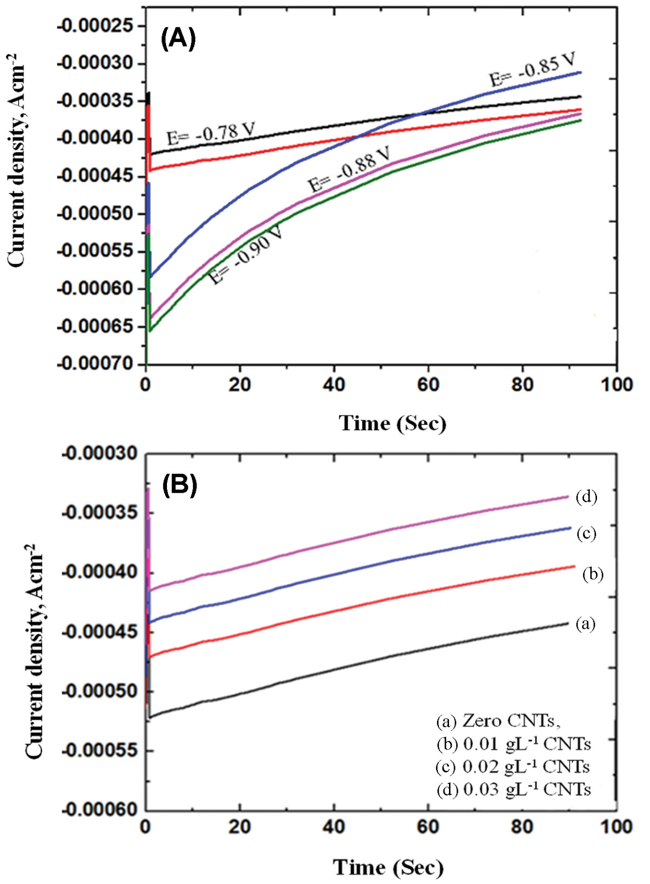

Fig. 6. Potentiation current-time transient during composite deposition, (A) at different deposition potentials (CNT=0.020 gL^{-1}) and (B) at different CNT concentrations (E=−0.85 V), where (a) Zero CNTs, (b) 0.01, (c) 0.02, and (d) 0.03 gL^{-1} CNTs.

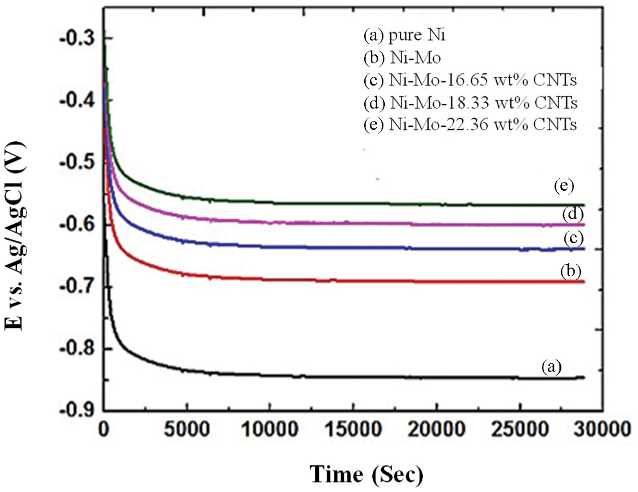

Fig. 7. The open circuit potential vs. time of NiMo alloy coating and NiMoCNTs coatings in 3.5% NaCl solution, where, (a) pure Ni, (b) Ni-Mo, (c) Ni-Mo-16.65 wt% CNTs, (d) Ni-Mo-18.33 wt% CNTs, and (e) Ni-Mo-22.36 wt% CNTs.

amperometry (current-time transient). Fig. 6(A) illustrates the typical potentiostatic i-t transient for NiMoCNT composites measured at a PtDE at different deposition potentials. The ascending component of the curve shows an increase in current as the electroactive region grows, either as individual nuclei grow (instantaneous growth) or as the number of nuclei grows (progressive growth). When the exposed surface gets totally saturated, the current transients settle out. The values of the observed instantaneous current dramatically increase as the cathodic potential becomes increasingly negative. The good linearity of the current with time in the first few seconds as the potential is becoming more negative indicate that under the experimental conditions, the NiMoCNTs deposit is caused by a mechanism in which instantaneous nucleation is followed by three-dimensional growth under charge transfer control [32]. At a deposition potential of –0.85 V, Fig. 6(B) depicts typical potentiostatic i-t transients observed during Ni(II) and Mo(VI) reduction in the absence and presence of CNTs. According to the data, the transient is characterized by a rapid increase in current as the electroactive area develops, before reaching a maximum and then progressively decreasing. Metal nucleation and phase growth on a Pt electrode produce such transients, and nucleation growth is not regarded to be a diffusion-controlled process.

7. Corrosion Behavior

The open circuit potential, electrochemical impedance spectroscopy (EIS), and anodic polarization techniques were utilized to investigate the corrosion behavior of a NiMoCNTs nanocomposite formed on a steel substrate in a 3.5% NaCl.

7-1. Open Circuit Potential

Fig. 7 shows the variation of free corrosion potential of NiMo and NiMo containing different contents of MWCNTs in 3.5% NaCl solution in open circuit conditions. The data illustrate that the composite that contained high MWCNT content (NiMo-22.36%wt CNTs) had nobler potentials than that containing lower MWCNT content. The high value of the potential for all of these samples at the beginning of immersion can be explained by the time necessary for the NaCl solution to reach the electrode surface by diffusion. The above result confirms that the composite containing high MWCNT content has higher corrosion resistance than composite

Table 7. Electrochemical parameters R_s and R_{ct} deduced from the Nyquist plot

Sample	Solution resistance R_s (Ω)	Charge transfer resistance R_{ct} (Ω)
NiMo	5.0	553.8
NiMo-16.65 wt% CNT	6.05	606.35
NiMo-18.33 wt% CNT	6.6	910.4
NiMo-22.36 wt% CNT	7.5	1,369.6

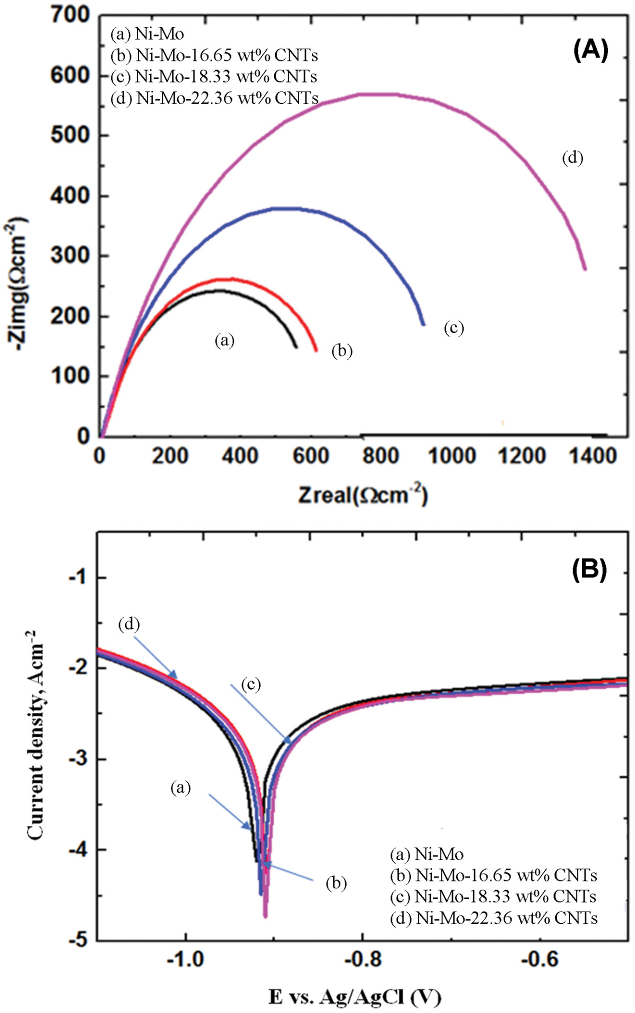

Fig. 8. Electrochemical techniques to investigate the corrosion behavior of NiMo alloy coating and NiMoCNTs coatings, (a) Ni-Mo, (b) Ni-Mo-16.65 wt% CNTs, (c) Ni-Mo-18.33 wt% CNTs, and (d) Ni-Mo-22.36 wt% CNTs in 3.5% NaCl solution, (A) Nyquist plot and (B) The potentiodynamic polarization curve.

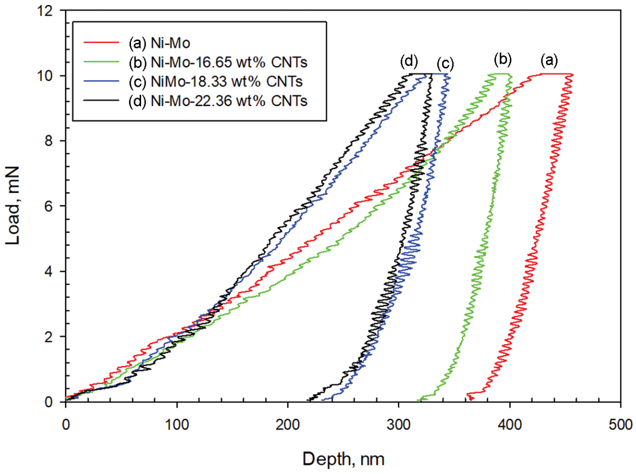

Fig. 9. Nanoindentation load-displacement curves (P-h curve) of the investigated samples.

containing lower MWCNT content.

7-2. Electrochemical Impedance Spectroscopy

Fig. 8(A) depicts the corrosion behavior of NiMo and NiMoCNT composite deposits in 3.5 wt% NaCl solutions at their respective open circuit potentials using the electrochemical impedance approach, and Table 7 summarizes the derived electrochemical parameters. All of the curves appear to be the same, with a single semicircle indicating the charge-controlled reaction in the high-frequency zone. Furthermore, the presence of a single semi-circle in the Nyquist plots indicates that deposit solution interfaces exhibit charge transfer behavior and that the corrosion process of these coatings is characterized by a single time constant ($\tau = R_{ct}C_{dl}$), implying the presence of a double layer at the deposit/electrolyte interface. The high charge transfer resistance (R_{ct}) values for the currently examined NiMoCNT composite coating compared to the NiMo coating imply that the composite deposits have a stronger corrosion protecting capacity.

7-3. Anodic Potentiodynamic Polarization

In a 3.5 percent NaCl solution, the corrosion behavior of the composites with varying CNTs concentration was investigated using an anodic potentiodynamic polarization measurement, as shown in Fig. 8(B). The curves were obtained by scanning the potential at a rate of 5 mV/s towards less negative potentials. As can be seen, all of the samples examined demonstrate active-passive behavior. Table 8 shows the I_{corr} (corrosion current density) and E_{corr} (corrosion potential) values obtained by fitting the anodic and cathodic Tafel regions of the potentiodynamic polarization curve with linear Tafel fitting. In the case of samples prepared with a high MWCNT content, the corrosion current I_{corr} declines and the E_{corr} shifts to a more positive potential value. The above finding suggests that the composite with a high concentration of MWCNT has a slightly higher corrosion resistance than the composite covered without MWCNT, leading to a decline in the composite's corrosion rate.

Table 8. Electrochemical parameters obtained after anodic potentiodynamic polarization of composite deposits in 3.5% NaCl solution

The parameters	NiMo alloy	NiMo-16.65 wt% CNTs	NiMo-18.33 wt% CNTs	NiMo-22.36 wt% CNTs
Ba (V/decade)	1.308	1.55	1.7	1.763
Bc (mV/decade)	346.6	293.7	305	288.8
$-E_{corr}$ (mV)	920.8	908.8	914.4	909.9
I_{corr} (μA)	4.834	4.781	4.601	4.547
Corr rate (mpy)	2.472	2.445	2.353	2.326
ChiSq	10.99	4.138	6.194	4.842

Table 9. The nanoindentation parameters of the NiMo coated steel and NiMoCNTs nanocomposite coated steel

Parameters	Steel coated sample by			
	NiMo	NiMo-16.65 wt%CNTs	Ni Mo-18.33 wt%CNT	Ni Mo-22.36 wt%CNTs
Hardness, (Gpa)	2.366	2.96	4.31	4.69
Young's modulus (Gpa)	77.5	123.45	116.39	135.50
h_f/h_{max}	0.81	0.80	0.68	0.66
Elastic modulus (E^*) (Gpa)	77.84	124.32	117.123	136.64
Reduced modulus (Er) (Gpa)	79.295	121.30	115.06	131.70
Elastic recovery	0.098	0.08	0.123	0.120
Elastic limit of strain (H/E_r)	0.0299	0.0244	0.037	0.036
Resistance to the plastic indentation (H^{*3}/E^2)	0.002	0.002	0.0058	0.0059
Elasticity index W_e/W_t	0.2296	0.23	0.40	0.38

8. Mechanical Properties by Nanoindentation

Nanoindentation was used to compare the mechanical properties of NiMo coated steel with NiMoCNTs nanocomposite-coated steel generated under ideal circumstances (25 °C, pH 3.5, current density 5.5×10^{-2} Acm^{-2}, and 0.03 gL^{-1} CNTs). Fig. 9 displays load-displacement curves (P-h curve). The data in Fig. 9 shows that the maximum depth of the indentor for NiMo coated steel is 457.21 nm, while the maximum depth of the indenter for NiMoCNTs composite coated steels with 0.01, 0.02, and 0.03 gL^{-1} CNTs is 401.94, 346.53, and 330.30 nm, respectively, indicating that the hardness of NiMoCNTs composite-coated steel is higher than that of NiMo. The highest hardness of NiMoCNTs composite coated steel was 4.69 GPa, while NiMo coated steel had a hardness of 2.37 GPa. Because the thickness of the coating films should be more than the maximum indentation depth to restrict the effect of the substrate on the mechanical characteristics of thin films, the range of indentation depths (457.21-330.30 nm) was kept.

Table 9 shows the nanoindentation parameters: hardness (H), reduced modulus (Er), elastic recovery, resistance to plastic indentation (H^{*3}/E^2), and elastic limit of strain (H/Er). The ratio between hardness and reduced modulus (H/Er), which refers to the elastic limit of strain and the elastic modulus, was calculated using the equation $E/(1-\nu^2)$, where E, Young's modulus, and ν Poisson's ratio were used. The results showed an improvement in resistance to plastic indentation (H^{*3}/E^2) ratio, which was in contrast to the behavior of the elastic modulus, and the improvement in (H^{*3}/E^2) ratio returned to an increase in hardness. The data suggests that the inclusion of CNTs into the NiMo matrix has a strong effect compared with the pure NiMo. The strengthening of CNTs in the NiMo matrix may be responsible for the increased hardness of NiMoCNTs coatings, and the enhancement is congruent with the Hall-Petch connection [18]. The nanoindentation curves in NiMoCNTs steel coated show that these coatings have higher penetration resistance than pure NiMo coatings with lower h_m values (the maximum depth an indenter can penetrate in the coating). Furthermore, the NiMoCNTs coatings have a lower h_f (residual hardness impression depth with unloading state in the coating). As shown in Table 9, the relationship between h_f/h_{max} and the elasticity index W_e (elasticity work)/W_t (total work of indentation) explains elasticity behavior through hardness contact, and the results show plasticity behavior for NiMoCNTs nanocomposite coated steel when compared to pure NiMo coated steel (W_e/W_t~0.4).

CONCLUSIONS

The NiMo coatings and CNT-based nanocomposites were successfully electrodeposited galvanostatically onto steel surfaces. The thickness of the nanocomposite obtained was found to be in the range of 7-11 μm depending on the applied current density and CNTs content. The results proved that the MWCNTs have a synergetic impact in promoting the properties of Ni-Mo thin films. It is clear that as the concentration of CNTs in the electrolyte increases, the weight percent of CNTs co-deposited in the NiMo matrix also increases, peaking at 22.36 wt% at 0.03 gL^{-1}. Furthermore, the findings indicate that the Mo content of the coating is reduced when CNTs are present. In comparison to a NiMo coating without CNTs, the composite incorporating CNTs exhibits better corrosion resistance. The incorporation of CNTs into the NiMo matrix explores a catalytic impact on Mo(VI) and Ni(II) reduction at the steel surface. The Tafel kinetics parameters show that the increase in temperature and the stirring rate catalyze the electrodeposition process, while the increase in pH inhibits it. The microhardness of NiMoCNT composite-coated steel is better than that of NiMo, and the highest microhardness of the prepared nanocomposite was 4.69 GPa, while pure NiMo coated steel had a value of 2.37 GPa.

REFERENCES

1. F. V. Ferreira, W. Franceschi, B. R. C. Menezes, A. F. Biagioni, A. R. Coutinho and L. S. Cividanes, *Synthesis, characterization, and applications of carbon nanotubes*, Elsevier Inc. (2018).
2. Z. Yang, H. Xu, Y. L. Shi, M. K. Li, Y. Huang and H. L. Li, *Mater. Res. Bull.*, **40**(6), 1001 (2005).
3. L. Shi, C. F. Sun, P. Gao, F. Zhou and W. M. Liu, *Surf. Coat. Technol.*, **200**(16-17), 4870 (2006).
4. C. Guo, Y. Zuo, X. Zhao, J. Zhao and J. Xiong, *Surf. Coat. Technol.*, **201**(24), 9491 (2007).
5. W. Fan, *Graphene-carbon nanotube hybrids for energy and environmental applications-springer briefs in molecular science*, Springer Verlag, Singapore (2017).
6. V. N. Popov, *Mater. Sci. Eng. R Rep.*, **43**(3), 61 (2004).
7. A. Wang, X. Chen, L. Cheng, X. Shen, W. Zhu, L. Lia and J. Pang,

J. Mater. Chem. A, **8**(34), 17621 (2020).

8. S. S. Karade, A. S. Nimbalkar, J. H. Eum and H. Kim, *RSC Adv.*, **10**(66), 40092 (2020).
9. A. Zarebidaki and S. R. Allahkaram, *J. Alloys Compd.*, **509**(5), 1836 (2011).
10. A. Esawi and K. Morsi, *Compos. Part A Appl. Sci. Manuf.*, **38**(2), 646 (2007).
11. S. Tailor, R. Mohanty and P. Soni, *J. Mater. Sci. Surf. Eng.*, **1**(1), 15 (2013).
12. J. Martinsen, R. A. Figat and M. W. Shafer, *MRS Online Proc. Library*, **32**, 145 (1984).
13. Z. A. Hamid and R. A. El-Adly, *Plat. Surf. Finish.*, **86**(5), 136 (1999).
14. Z. A. Hamid, *Surf. Interface Anal.*, **35**(6), 496 (2003).
15. A. R. Barron and M. R. Khan, *Adv. Mater. Process.*, **166**(10), 41 (2008).
16. Z. Abdel Hamid, M. Refai, R. M. El-kilani and G. E. M. Nasr, *J. Mater. Sci.*, **56**(25), 14096 (2021).
17. M. Refai, Z. Abdel Hamid, R. M. El-kilani and G. E. M. Nasr, *J. Mater. Eng. Perform.*, **30**(3), 1851 (2021).
18. M. Refai, Z. A. Hamid, R. M. El-kilani and G. E. M. Nasr, *Chem. Pap.*, **75**, 139 (2021).
19. N. F. El Boraei and M. A. M. Ibrahim, *Mater. Chem. Phys.*, **285**, 126138 (2022).
20. C. M. P. Kumar, A. Lakshmikanthan, M. P. G. Chandrashekarappa, D. Y. Pimenov and K. Giasin, *Coatings*, **11**, 712 (2021).
21. Z. A. Hamid, A. Y. El-Etre and M. Fareed, *Anti-Corrosion Methods Mater.*, **64**(3), 315 (2017).
22. Z. Abdel Hamid, H. B. Hassan and M. Sultan, *Anti-Corrosion Methods Mater.*, **67**(1), 38 (2020).
23. J. Kubisztal, A. Budniok and A. Lasia, *Int. J. Hydrogen Energy*, **32**(9), 1211 (2007).
24. W.-F. Chen, K. Sasaki, C. Ma, A. I. Frenkel, N. Marinkovic, J. T. Muckerman, Y. Zhu and R. R. Adzic, *Angew. Chem. - Int. Ed.*, **51**(25), 6131 (2012).
25. N. F. El Boraei and M. A. M. Ibrahim, *Surf. Coat. Technol.*, **347**, 113 (2018).
26. J. H. Liu, J. X. Yan, Z. L. Pei, J. Gong and C. Sun, *Surf. Coat. Technol.*, **404**, 126476 (2020).
27. E. Beltowska-Lehman and P. Indyka, *Thin Solid Films*, **520**(6), 2046 (2012).
28. M. Donten, H. Cesiulis and Z. Stojek, *Electrochim. Acta*, **50**(6), 1405 (2005).
29. A. P. Grosvenor, M. C. Biesinger, R. S. C. Smart and N. S. McIntyre, *Surf. Sci.*, **600**(9), 1771 (2006).
30. M. A. M. Ibrahim, *J. Appl. Electrochem.*, **36**(3), 295 (2006).
31. N. F. El Boraei, M. A. M. Ibrahim and M. A. Naghmash, *J. Phys. Chem. Solids*, **167**, 110714 (2022).
32. M. Schlesinger and M. Paunovic, *Modern electroplating fifth edition*, Fifth Edit. NY: Ajohn Wiley&sons, Inc., Publication (2011).